

Radial Diffusion of Geomagnetically Trapped Protons Observed by the Galileo Energetic Particle Detector

Naser Alinejad

Nuclear Fusion Research Center, Atomic Energy Organization of Iran, Tehran, Iran

and Thomas P. Armstrong

Fundamental Technologies, LLC, 2411 Ponderosa, Suite A, Lawrence, KS 66046

The Galileo spacecraft encountered the Earth once on December 8, 1990 (Earth-I), and again on December 8, 1992 (Earth-II). These flybys provided excellent opportunities to evaluate the performance of the Energetic Particle Detector (EPD) and establish analysis procedures in a relatively well-known environment. Further, because Galileo's Earth flyby trajectories were very rapid and nearly radial, the radiation belt measurements provided an excellent “snapshot” of trapped radiation. Because of the rapid flyby and the 20 second spin period of Galileo, great care had to be taken to remove time aliasing from the pitch angle distributions. Large anisotropies were also present due to intrinsic density gradients. Spherical harmonics were fitted to the pitch and phase distributions in order to obtain fluxes from which phase space densities could be computed. The phase space density (PSD) was calculated from the fitted count rate for the particles (protons) that conserve the first and second adiabatic invariants. The values of 10.0, 15.0, 20.0, 25.0 30.0, 35.0, 40.0, 45.0, and 50.0 MeV/G were used for the first adiabatic invariant, and the values of 0.10, 0.15, 0.20, 0.25, 30.0, and 0.50 $G^{0.5} R_E$ were used for the second adiabatic invariant to determine the PSD from Earth-I and Earth-II observations. The extracted PSDs were examined for radial

diffusion. Results show there is no unique global dependency of the diffusion coefficient to L, except for a limited region of the first and second adiabatic invariants.

Introduction

Diffusion of geomagnetically trapped particles has been studied by *Nakada and Mead* [1965]; *Falthammar* [1966, 1968, 1970]; *Haerendel* [1968, 1970]; *Birmingham et al.* [1968]; *Roederer* [1968a, b]; *Walt* [1970]; *Williams* [1970]; *Cornwall* [1972]; *Croley et al.* [1976]; *Spjeldvik* [1977]; *Holzworth and Mozer* [1979]; *Westphalen and Spjeldvik* [1982]; *Jentsch* [1984]; *Riley and Wolf* [1992]; *Lui* [1993]; and *Sheldon* [1994]. *Falthammar* [1966] applied the one-dimensional Fokker-Planck equation to particles moving near the equatorial plane and found two different results for the diffusion coefficient depending on the assumed characteristics of the magnetic impulses compared to the azimuthal drift period. For randomly repeated pulses with very short rise time and very long duration, the result was $D \propto r^{10}$, and for pulses not much longer than the drift period the result was $D \propto \mu^2 r^6$. *Spjeldvik* [1977] worked on a numerical solution of the Fokker-Planck equation by imposing boundary conditions to explain the equilibrium structure of equatorial radiation belt protons and compared the results with observations. The steady state transport equation at an arbitrary pitch angle has been used by *Jentsch* [1984] to study the radial distribution of radiation belt protons.

A summary of observational evidence on radial diffusion of geomagnetically trapped particles was given by *Roederer* [1968a]. The theoretical and experimental values of the radial diffusion coefficients have been summarized by *Falthammar* [1970] and updated by *Walt* [1971] and then by *Holzworth and Mozer* [1979]. Radial diffusion coefficient values derived from both theoretical and

experimental sources, as updated by *Holzworth and Mozer* [1979], are given in Figure 1. Results for D_{LL} are labeled by numbers and correspond to the investigations organized historically and shown in the figure. Because Figure 1 includes a wide range of particle energies and calculation methods, the spread of values for the diffusion coefficient is several orders of magnitude at a given L-value. Despite the spread of D_{LL} values, Figure 1 suggests that radial diffusion occurs at rates which generally diminish with decreasing L-value as mentioned by Walt. A summary of different methods of determining D_{LL} is given by *Lanzerotti et al.* [1978], and estimated radial diffusion coefficients from measurements of electric and magnetic field fluctuations are compared by *Lanzerotti and Wolfe* [1980; see Figure 2 of that paper].

In this experimental investigation, geomagnetically trapped protons of 22 keV to 3.20 MeV have been studied for the region $L=1.5$ to $L=10.0$ based on observations by the Galileo spacecraft during the Earth-I (December 8, 1990) and Earth-II (December 8, 1992) encounters. This work differs from others in that it covers the entire radiation belt region for a broad range of proton energies and includes treatment of off-equatorial mirroring particles. The extracted phase space density (PSD) from Galileo Energetic Particle Detector (EPD) observed count rates was compared to that from the NASA AP8 model, and the result was reported by *Alinejad and Armstrong* [1997] (hereafter referred to as paper-I). In this current paper, we will examine the Galileo PSD of protons for radial diffusion by violation of the third adiabatic invariant while conserving the first two adiabatic invariants.

The main mission of the Galileo spacecraft was to study the Jupiter system, including the galilean satellites, the Jovian atmosphere, and the Jovian magnetosphere. The trajectory of the Galileo spacecraft was designed to use a Venus-Earth-Earth gravity assist (VEEGA) to gain enough energy and the desired trajectory to reach Jupiter. The VEEGA trajectory used one gravity-assisted

flyby of Venus and two gravity-assisted flybys of Earth. The Galileo spacecraft carried an Energetic Particle Detector (EPD) which was designed to measure the population of particles. The Galileo mission, trajectory, instrumentation, and EPD instrument are described in paper-I.

To be able to determine the pitch angle along the spacecraft trajectory, a local magnetic field is required. During the second Galileo Earth encounter, geomagnetic field observations were saturated at closest approach; therefore, the Tsyganenko-87 magnetospheric magnetic field analytical model [Tsyganenko, 1987] was used for analysis purposes for the second Earth flyby. A brief introduction to this model and its validity are given in paper-I.

Method and Formulation

Data from the Galileo project were received in the form of particle count rates versus time in sixteen sectors for each spacecraft spin in the case of the proton energy channels. To be able to analyze these data, the spacecraft orientation was transformed into the magnetic coordinates. In this coordinate transformation, the spacecraft spin axis was transformed to the local magnetic field direction. In this case, the angle between the look direction and the Z-axis gives the particle's pitch angle, α . Ephemeris data was used to determine the phase angle of the look direction. The X-axis was chosen to be in the plane formed by the Z-axis and the spacecraft-Earth line, and the Y-axis completes the Cartesian coordinate. Projection of the look direction on the X-Y plane from the X-axis gives the phase angle, ϕ . In this transformation, count rate is a function of energy (E), pitch angle (α), and azimuthal angle (ϕ), at each position (L); that is

$$R_{ij}=R(E_i,\alpha_j,\phi_j,L) \quad (1)$$

where i indicates the energy channel and j indicates the sector position. As the spacecraft spins, the direction of the detector changes and the spacecraft maps gyrocenters located within 2 gyroradii. If two points are connected with a line passing through the center of the loop, corresponding gyrocenters of these two points will be separated by 2 gyroradii. Since count rates differ because of the gyrocenter locations, loops are an indication of the spatial gradient. The presence of the spatial gradient in each spin does not allow for simple linear interpolation with respect to the pitch angle; this is one of the reasons to fit the data to the function which depends on phase angle as well as on pitch angle. Since the energy and pitch angle of the particles (protons) are known for the first and second adiabatic invariants (which are conserved), the corresponding phase space density, f , can be deduced from the flux. The detailed procedure of calculation of the PSD at constant μ and K from the count rate, which was fitted to the associated Legendre function by a χ^2 minimization method, is given in paper-I.

In summary, the spin averaged count rates were organized in three motor position (step) groups so data were linked from one step to another. Ranges of the first two adiabatic invariants were determined from the spacecraft position and the intersection of magnetic field lines with the Earth's surface. Values of 10.0, 15.0, 20.0, 25.0, 30.0, 35.0, 40.0, 45.0, and 50.0 MeV/G were chosen for the first adiabatic invariant, μ , and values of 0.10, 0.15, 0.20, 0.25, 0.30, and 0.50 $G^{0.5} R_E$ were chosen for the second adiabatic invariant, K . Energy, E^* , and pitch-angle, α^* , were calculated for each pair of these two adiabatic invariants. Energy was bounded between geometrical mean energies of two consecutive energy channels, and associated Legendre function was fitted to data of each proton channel. Coefficients from each fitting along with α^* and gyrophase were used to calculate the differential flux of each channel and then interpolated for energies to find the

differential flux corresponding to E^* . The phase space density was determined from differential flux.

For the higher values of the second adiabatic invariant, $K > 5.0$, there were not many data points obtained after the spherical harmonic was fitted to the observed data, because for higher values of K the pitch angle of particles increases accordingly. Therefore, most particles mirror before reaching the spacecraft at higher local latitude and causing a reduction in the particle's flux. Also, there was a restriction on data in that only points which were larger than or equal to 50 percent of the largest value in the group of steps were retained. This restriction eliminated most of the data for the higher energy particles. For each pair of the first and second adiabatic invariants, corresponding phase space densities were calculated by the method that was discussed in paper-I. There are four sets of data corresponding to inbound and outbound of Earth-I and inbound and outbound of Earth-II. With conservation of the first two adiabatic invariants, each set covers a limited region of the radiation belts. To have better coverage of the radiation belt zone, all four sets were combined and analyzed as one set of data. Hence the combined four sets of phase space density will be referred to as just phase space density.

To analyze data by using equation (2), we introduce an empirical function $f(L)$ with three parameters as

$$F = \ln f = b_1 + b_2 \ln(L - b_3) \quad (2)$$

This form has been found to fit the observations as will be displayed in Figures 2 to 6. The last term in this equation is the logarithmic function, and the argument must be positive values. This condition implies a restriction on the third parameter; therefore b_3 must satisfy

$$b_3 < L_{\min} \quad (3)$$

There are no restrictions on the other parameters. Three parameters, b_1 , b_2 and b_3 , are determined from fitting the empirical function to the phase space density by the χ^2 minimization method. These parameters are tabulated in Table 1. The dashed lines in Figures 2 to 6 show the fits with parameter values given in Table 1.

From analysis of all pairs of the first two adiabatic invariants, we show here, in Figures 2 through 6, only a few graphs of phase space densities and corresponding fitted points versus L . These graphs are for values of the first adiabatic invariant, $\mu = 10.0$ to 50.0 by step 10.0 which are paired with two extreme values of the second adiabatic invariant, $K=0.10$ and $K=0.50$. On all of these graphs observational data is marked by open triangles for $K=0.10$ and by open squares or circles for $K=0.50$, and corresponding points from fitting the introduced empirical function (equation (2)) are represented by solid triangles and solid squares connected by a dotted line. Each of these figures consists of two graphs; while each graph corresponds to the same value of the first adiabatic invariant, the upper graph is for $K=0.10$ and the lower graph corresponds to $K=0.50$. The values of the first two invariants are shown on the graphs.

Figure 2 represents the PSD and fitted points versus L for $\mu=10.0$ and $K=0.10$ in the upper graph and $K=0.50$ in the lower graph. In the upper graph, observed data are scattered around the fitted points. The PSD is less than the fitted points at region $L < 2.0$ and exceeds the fitted points at region $2.0 \leq L \leq 3.0$, becomes less than fitted points at region $3.0 < L < 4.2$, and again is higher at $L=4.4$ and $L=5.3$. On the other hand, in the lower graph there is good agreement between observation and empirical function for region $L \leq 2.0$, and observation is higher than fitted points

for region $2 < L \leq 4.2$ and then decreases at region $L \geq 5.8$. As mentioned before, the represented PSD is a collection of four sets of data from inbound and outbound of Earth-I and Earth-II, which were observed at different times and different geomagnetic latitudes, which in turn causes data from the different sets not to overlap with each other.

The upper graph of Figure 3 represents PSD and fitted points for $\mu = 20.0$ and $K=0.10$, and the lower graph is for $K=0.50$. In the upper graph, PSD and fitted points agree with each other except for region $2.5 \leq L \leq 3.1$. In the lower graph, data exceeds the fitted points at $3.6 \leq L \leq 4.2$ and is less than fitted points at region $3.8 \leq L \leq 6.4$.

In Figure 4, which is for $\mu= 30.0$ and $K=0.10$ (upper graph) and $K=0.50$ (lower graph), data are scattered around fitted points at region $5.0 \leq L \leq 7.5$. This happened because at the time of the inbound of the Earth-I encounter, there was a geomagnetic storm which affected higher energy particles more. This effect is pronounced in Figure 5 and Figure 6 in the case of $K=0.10$. We discussed the effect of the storm in more detail in paper-I. In the lower graph, data and fitted points are in relatively good agreement with each other. In both Figure 5 and Figure 6, data and fitted points match each other in the lower graphs, and data is scattered around fitted points in the upper graph, which is due to the geomagnetic storm effect mentioned earlier. Despite the scatter introduced by secular variation, the empirical form of the PSD (function shown in equation (3)) is reasonably well-behaved.

Table 1 summarizes the values of three parameters, b_1 , b_2 , and b_3 , for the full range of adiabatic invariants for which we have coverage. Figure 7 shows $\exp(b_1)$ versus μ for the two extreme observed values of L . Note from Equation (3) that this expression sets the magnitude of the PSD and that the magnitude of the PSD falls much more rapidly with increasing μ for off-equatorial protons ($K=0.5$) than for those closer to the equator ($K=0.1$). At $\mu = 10$ MeV/gauss, for example,

the PSD for $K = 0.5$ is only about a factor of 2 smaller than that for $K = 0.1$, while at 50 MeV/gauss the PSD for $K = 0.5$ is more than a factor of 100 smaller than that for $K = 0.1$. This result illustrates the fact that PSDs for higher energies (corresponding to higher μ values) diminish with increasing K much more rapidly than for lower energies. Figure 8 shows the parameter b_2 representing the exponent of the L -dependence of the PSD. We show how b_2 varies with the first invariant, μ , at the extreme observed values of the second invariant, K . The points for $K=0.1$ all lie above those for $K=0.5$ at the same values of μ , showing that the PSD for protons mirroring closer to the equator ($K=0.1$) depends more strongly on L than for those mirroring further from the equator ($K=0.5$). For both values of the second invariant, $K=0.1$ and $K=0.5$, the L -dependence of PSD becomes much stronger at low values of the first invariant. Note that all values of b_2 are positive, which shows that the PSD increases monotonically with L for all values of first and second adiabatic invariants.

The fitting results for the final parameter, b_3 , of equation (2) are shown in Figure 9. Inspection of the patterns in Figure 9 suggests that this parameter is either not well determined by our data set, may not have easily interpreted physical significance, or that our presentation of it does not reveal the variations effectively. From the form of equation (3), it is evident that b_3 is a parameter of convenience introduced to allow the PSDs to be represented more compactly and accurately than would otherwise be the case. It's more easily understood as a zero offset of the L scale. We do not attempt to explain or rationalize it here.

Since phase space density f is known from the fitting procedures, which was explained in paper-I, we can use the quadrature (spatial) method [*Schulz and Lanzerotti, 1974*]. If we let $F \equiv \ln f$ then the radial diffusion equation can be written as

$$\frac{\partial F}{\partial t} = \left[L^2 \frac{\partial}{\partial L} \left(\frac{D_{LL}}{L^2} \right) \right] \frac{\partial F}{\partial L} + D_{LL} \left[\frac{\partial^2 F}{\partial L^2} + \left(\frac{\partial F}{\partial L} \right)^2 \right] - \frac{1}{\tau} \quad (4)$$

for constant μ and K ; τ is the particle lifetime and represents the loss and/or source term.

Taking the first and second derivatives of F (equation (2)) with respect to L , we have

$$\frac{\partial F}{\partial L} = \frac{b_2}{L - b_3} \quad (5)$$

and

$$\frac{\partial^2 F}{\partial L^2} = \frac{-b_2}{(L - b_3)^2} \quad (6)$$

To proceed further in interpreting the PSDs it is necessary to introduce an assumed form of diffusion coefficient. Here we take a power law form in L .

Approach #1: Time Stationary Transport with Source and Loss for Power Law form of D_{LL}

Assuming the diffusion coefficient to be a power-law with respect to L :

$$D = D_0 L^n \quad (7)$$

and considering only a steady state condition

$$\frac{\partial f}{\partial t} = 0 \quad (8)$$

the steady state diffusion equation can be written as

$$\frac{1}{D_0 \tau L^n} = \frac{(n-2.0)}{L} \left[\frac{b_2}{L-b_3} \right] + \left[\frac{-b_2}{(L-b_3)^2} + \left(\frac{b_2}{L-b_3} \right)^2 \right] \quad (9)$$

The values of b_1 , b_2 , and b_3 are empirically determined from fitting the Galileo EPD observations. In this simplified transport equation with all mentioned assumptions, source and loss terms, represented by τ , and the transport rate, represented by “n” and D_0 , are coupled. Equation (9) is not sufficient to allow one to proceed without further information. To be able to use equation (9) one of the parameters, either “n” or $D_0\tau$, must be determined. Note here that if there are no sources or losses this would make the left hand side of equation (9) equal zero. The right hand side of equation (9) then would require a solution for n as

$$n = 2.0 + L \left[\frac{1-b_2}{L-b_3} \right] \quad (10)$$

The equation shows that n would depend on L, and that is undesirable. The preferred value for n is the one for which equation (9) is satisfied for all L values. Clearly, to match the requirement of the power law form of the L-dependence of the diffusion coefficient, some source or loss is required.

One possibility is to choose the value of n for which the source or loss term will be minimized for the entire radiation belt region, that is

$$L^2 \left[\frac{1}{D_0 \tau L^n} \right] \Delta L = \min \quad (11)$$

for all L's or

$$\sum_i \left| \frac{(n-2.0)}{L_i} \left[\frac{b_2}{L_i - b_3} \right] + \left[\frac{-b_2}{(L_i - b_3)^2} + \left(\frac{b_2}{L_i - b_3} \right)^2 \right] L_i^2 \Delta L_i \right| = \min \quad (12)$$

The reason to weight equation (11) or equation (12) by L^2 is to get more distinguishable values for different n. The behavior of this equation for different values of n is shown in Figure 10 for $\mu=10.0$ MeV/gauss and $K=0.10$ (gauss)^{1/2} R_E as a sample. The ordinate values of this graph are equal to equation (12). Here the value of n= -5 is the exponent of choice. This value of n is used in equation (9) to calculate the $(D_0 \tau)^{-1}$ term.

Since all four parameters in equation (9) are known, they are used to evaluate

$$\frac{1}{D_0 \tau} = \left(\frac{(n-2.0)}{L} \left[\frac{b_2}{L - b_3} \right] + \left[\frac{-b_2}{(L - b_3)^2} + \left(\frac{b_2}{L - b_3} \right)^2 \right] \right) L^n \quad (13)$$

which is actually the inverse of the diffusion coefficient multiplied by a particle's lifetime and represents the loss or source term. A sample graph of $(D_0 \tau)^{-1}$ versus L is shown in Figure 11 for

$\mu=10.0$ MeV/gauss and $K=0.10$ (gauss)^{1/2} R_E. Since in this graph logarithmic scale is used, the absolute value of $(D_0\tau)^{-1}$ is displayed. Loss and source are separately indicated on the graph. Subject to the assumptions of time stationary distributions and power law diffusion coefficient dependence of $D_{LL}=D_0L^5$, we calculate losses increasing approximately exponentially with decreasing distance from $L = 2.3 R_E$ inward to $L = 1.3 R_E$. Beyond $2.3 R_E$ this analysis results in a source of PSD peaking at about $2.8 R_s$ and diminishing approximately exponentially throughout the rest of the observed range in this study.

Table 2 shows the results for preferred n-values for all of the cases in this study. Variation of n versus μ for $K = 0.1$ and 0.3 (gauss)^{1/2} R_E is illustrated in Figure 12. Note that all of the n-values for $K = 0.1$ (gauss)^{1/2} R_E are smaller than the values for $K =$ (gauss)^{1/2} R_E for all of the first invariant values used here. The patterns in Figure 12 indicate a stronger dependence of diffusion coefficient on L for protons mirroring closer to the equator compared to those mirroring further from the equator. Also evident in Figure 12 is a sharp decrease in the value of n that occurs as the first invariant diminishes from 30 to 10 MeV/gauss. Above 30 MeV/gauss the results in Figure 12 suggest that radial diffusion of protons is much less strongly dependent on L. One is tempted to suspect that different processes may govern the transport of protons above 30 MeV/gauss compared to those below.

Approach #2: Determination of D_{LL} Considering Time Stationary Transport Without Loss or Source

To be able to determine the functional relation between L and D_{LL} , we consider the loss-free, source-free and stationary case of equation (2) which reads

$$\left[L^2 \frac{\partial}{\partial L} \left(\frac{D_{LL}}{L^2} \right) \right] \frac{\partial F}{\partial L} + D_{LL} \left[\frac{\partial^2 F}{\partial L^2} + \left(\frac{\partial F}{\partial L} \right)^2 \right] \quad (14)$$

By substitution for $\partial F/\partial L$ and $\partial^2 F/\partial L^2$ of equation (3), equation (14) reduces to

$$\frac{\partial}{\partial L} \left(\frac{D_{LL}}{L^2} \right) = \frac{D_{LL}}{L^2} \left(\frac{1-b_2}{L-b_3} \right) \quad (15)$$

The solution of this differential equation is

$$D_{LL} = CL^2 (L-b_3)^{1-b_2} \quad (16)$$

where C is a constant and can be determined from boundary conditions if parameters b_2 and b_3 are known.

In our case, to examine equation (16), we have used values for parameters b_2 and b_3 corresponding to extreme values as well as middle values of μ and K from Table 1. Results for pairs of the first two adiabatic invariants (10.0 and 0.10; 10.0 and 0.50; 30.0 and 0.10; 30.0 and 0.50; 50.0 and 0.10; 50.0 and 0.50) are shown in Figure 13. Values of μ and K corresponding to parameters b_2 and b_3 are also shown on the graph. The parameter C was set to unity in all cases. From Figure 13 it is clear that D_{LL} depends on μ as well as on K. In all cases of the first adiabatic invariant, as the value of the second adiabatic invariant increases, D_{LL} increases as well, which is an indication of dependency of D_{LL} on pitch angle.

Conclusion

The purpose of this work was to investigate the time stationary transport using two alternatives to determine the dependence of the diffusion coefficient on L . To be able to determine the relation between D and n , we give the results for n corresponding to each pair of the first two adiabatic invariants in tabular form (Table 2). As mentioned before, since there is no single value for n for all pairs of the first two adiabatic invariants, it is difficult to conclude any reasonable power-law dependency of the diffusion coefficient to L by conservation of the first and second adiabatic invariants except for higher values of the first adiabatic invariant ($\mu \geq 25.0$). Still in this region, n varies from -2.0 to 1.0. If we limit values of the first two adiabatic invariants to

$$25.0 \leq \mu \leq 40.0 \quad \text{and} \quad 0.15 \leq K \leq 0.25 \quad (17)$$

then we have better results, but this is not the case since we are trying to get a more general result. Unlike the magnetic and electric fluctuations, our results show weak dependency of the diffusion coefficient on L .

Figure 9 shows the dependency of the diffusion coefficient on both the first and second adiabatic invariants in the case of loss-free, source-free and stationary assumption of radial diffusion.

From the results of data analysis in the case of conservation of the first two adiabatic invariants, it is not possible to conclude that it is the formulation of the distribution of radiation belt particles by conservation of the first two adiabatic invariants or simplified radial diffusion equations that

fails. More information such as temporal variations and source and loss terms is needed in data analysis for more complete results.

Despite the behavior of n with respect to the first two adiabatic invariants in power law as well as variation of D_{LL} with respect to L in the second approach, it is difficult to determine the pattern of dependency of the diffusion coefficient to L . This is the reason that analysis of pure radial diffusion with conservation of the first two adiabatic invariants failed to define a single exponent for the radial diffusion coefficient. In a follow-up paper the new variable will be introduced to study diffusion, which will illustrate how one dimensional radial diffusion analysis can be improved.

Acknowledgments: This work has been supported by NASA under contract number 601714-0. We would like to thank NASA for their support and also thank the Galileo science team, the EPD team, and the MAG team for their data and help.

References

Alinejad, N., and T. P. Armstrong, Galileo Energetic Particle Detector observations of geomagnetically trapped protons, *J. Geophys. Res.*, **102**, 27053, 1997.

Birmingham, T. J., T. G. Northrop, and C. G. Falthammar, Charged particle diffusion by violation of the third adiabatic invariant, in *Physics of the Magnetosphere*, edited by R. L. Carovillano, J. F. McClay, and H. R. Radoski, pp. 660-677, Springer-Verlag, New York, 1968.

Cornwall, J. M., Radial diffusion of ionized helium and protons: A probe for magnetospheric dynamics, *J. Geophys. Res.*, **77**, 1756, 1972.

Croley, D. R., Jr., M. Schulz, and J. B. Blake, Radial diffusion of inner-zone protons: Observations and variational analysis, *J. Geophys. Res.*, **81**, 585, 1976.

Falthammar, C. G., On the transport of trapped particles in the outer magnetosphere, *J. Geophys. Res.*, **71**, 1487, 1966.

Falthammar, C. G., Radial diffusion by violation of the third adiabatic invariant, in *Earth's Particles and Fields*, edited by B. M. McCormac, pp. 157-169, Reinhold Book Corporation, New York, 1968.

Falthammar, C. G., Introductory survey of radiation belt diffusion, in *Particles and Fields in the Magnetosphere*, edited by B. M. McCormac, pp. 387-395, D. Reidel Publishing Company, Dordrecht, Holland, 1970.

Haerendel, G., Diffusion theory of trapped particles and the observed proton distribution, in *Earth's Particles and Fields*, edited by B. M. McCormac, pp. 171-191, Reinhold Book Corporation, New York, 1968.

Haerendel, G., On the balance between radial and pitch angle diffusion, in *Particles and Fields in the Magnetosphere*, edited by B. M. McCormac, pp. 416-428, D. Reidel Publishing Company, Dordrecht, Holland, 1970.

Holzworth, R. H., and F. S. Mozer, Direct evaluation of the radial diffusion coefficient near L=6 due to electric field fluctuations, *J. Geophys. Res.*, **84**, 2559, 1979.

Jentsch, V., The radial distribution of radiation belt protons: Approximate solution of the steady state transport equation at arbitrary pitch angle, *J. Geophys. Res.*, **89**, 1527, 1984.

Lanzerotti, L. J., and A. Wolfe, Particle diffusion in the geomagnetosphere: Comparison of estimates from measurements of magnetic and electric fluctuations, *J. Geophys. Res.*, **85**, 2346, 1980.

Lanzerotti, L. J., D. C. Webb, and C. W. Arthur, Geomagnetic field fluctuations at synchronous orbit: 2. Radial diffusion, *J. Geophys. Res.*, **83**, 3866, 1978.

Lui, A. T. Y., Radial transport of storm time ring current ions, *J. Geophys. Res.*, **98**, 209, 1993.

Nakada, M. P., and G. D. Mead, Diffusion of protons in the outer radiation belt, *J. Geophys. Res.*, **70**, 4777, 1965.

Riley, P., and R. A. Wolf, Comparison of diffusion and particle drift descriptions of radial transport in the Earth's inner magnetosphere, *J. Geophys. Res.*, **97**, 16865, 1992.

Roederer, J. G., Experimental evidence on radial diffusion of geomagnetically trapped particles, in *Earth's Particles and Fields*, edited by B. M. McCormac, pp. 143-155, Reinhold Book Corporation, New York, 1968a.

Roederer, J. G., Shell splitting and radial diffusion of geomagnetically trapped particles, in *Earth's Particles and Fields*, edited by B. M. McCormac, pp. 193-208, Reinhold Book Corporation, New York, 1968b.

Schulz, M., and L. J. Lanzerotti, *Particle Diffusion in the Radiation Belts*, Springer Verlag, New York, 1974.

Sheldon, R. B., Ion transport and loss in the Earth's quiet ring current: 2. Diffusion and magnetosphere coupling, *J. Geophys. Res.*, **99**, 5705, 1994.

Spjeldvik, W. N., Equilibrium structure of equatorially mirroring belt protons, *J. Geophys. Res.*, **82**, 2801, 1977.

Tsyganenko, N. A., Global quantitative models of the geomagnetic field in the cislunar magnetosphere for different disturbance levels, *Planet. Space Sci.*, **35**, 1347, 1987.

Walt, M., Radial diffusion of trapped particles, in *Particles and Fields in the Magnetosphere*, edited by B. M. McCormac, pp. 416-428, D. Reidel Publishing Company, Dordrecht, Holland, 1970.

Walt, M., Radial diffusion of trapped particles and some of its consequences, *Rev. Geophys. Space Phys.*, **9**, 11, 1971.

Westphalen, H., and W. N. Spjeldvik, On the energy dependence of the radial diffusion coefficient and spectra of inner radiation belt particles: Analytic solution and comparison with numerical results, *J. Geophys. Res.*, **87**, 8321, 1982.

Williams, D. J., Trapped protons ≥ 100 keV and possible sources, in *Particles and Fields in the Magnetosphere*, edited by B. M. McCormac, pp. 396-409, D. Reidel Publishing Company, Dordrecht, Holland, 1970.

Figure Captions

Figure 1. Radial diffusion coefficients derived by various methods and by many experimenters (from *Holzworth and Mozer* [1979], Figure 5; copyright American Geophysical Union). Solid lines are derived with some assumptions from experimental data, while dashed lines are theoretical determinations. The sources are given in the inset.

Figure 2. Phase space density and fitted points vs L for $\mu = 10$ MeV/gauss and $K = 0.1$ and 0.5 (gauss)^{1/2} R_E. Dashed lines show the results of least squares fits to the form of equation (3) and the solid symbols evaluate that fit at the tabulated L-values.

Figure 3. Phase space density and fitted points vs L for $\mu = 20$ MeV/gauss and $K = 0.1$ and 0.5 (gauss)^{1/2} R_E. Dashed lines show the results of least squares fits to the form of equation (3) and the solid symbols evaluate that fit at the tabulated L-values.

Figure 4. Phase space density and fitted points vs L for $\mu = 30$ MeV/gauss and $K = 0.1$ and 0.5 (gauss)^{1/2} R_E. Dashed lines show the results of least squares fits to the form of equation (3) and the solid symbols evaluate that fit at the tabulated L-values.

Figure 5. Phase space density and fitted points vs L for $\mu = 40$ MeV/gauss and $K = 0.1$ and 0.5 (gauss)^{1/2} R_E. Dashed lines show the results of least squares fits to the form of equation (3) and the solid symbols evaluate that fit at the tabulated L-values.

Figure 6. Phase space density and fitted points vs L for $\mu = 50$ MeV/gauss and $K = 0.1$ and 0.5 (gauss)^{1/2} R_E. Dashed lines show the results of least squares fits to the form of equation (3) and the solid symbols evaluate that fit at the tabulated L-values.

Figure 7. Variation of the PSD fit coefficient, $\exp(b_1)$, versus first invariant, μ , for the extreme observed values of $K=0.1$ and 0.5 (gauss)^{1/2} R_E.

Figure 8. Variation of PSD fit coefficient b_2 versus first invariant, μ , for the extreme observed values of $K=0.1$ and 0.5 (gauss)^{1/2} R_E.

Figure 9. Variation of PSD fit coefficient b_3 versus first invariant, μ , for all observed values of $K=0.1, 0.15, 0.2, 0.25, 0.3,$ and 0.5 (gauss)^{1/2} R_E.

Figure10. Behavior of equation (12) with respect to n for $\mu=10.0$ MeV/gauss and $K=0.10$ (gauss)^{1/2} R_E.

Figure11. Source and loss versus L for $\mu=10.0$ MeV/gauss and $K=0.10$ (gauss)^{1/2} R_E.

Figure 12. Variation of preferred n values for power law diffusion versus first invariant, m , for $K = 0.1$ and 0.3 (gauss)^{1/2} R_E.

Figure13. Radial diffusion coefficients versus L for different values of parameters b_2 and b_3 (equation (3)) corresponding to different pairs of the first two adiabatic invariants. The values of

adiabatic invariants are shown on the graph. The first value of each pair corresponds to the first adiabatic invariant and the second value of each pair corresponds to the second adiabatic invariant (Table 1).

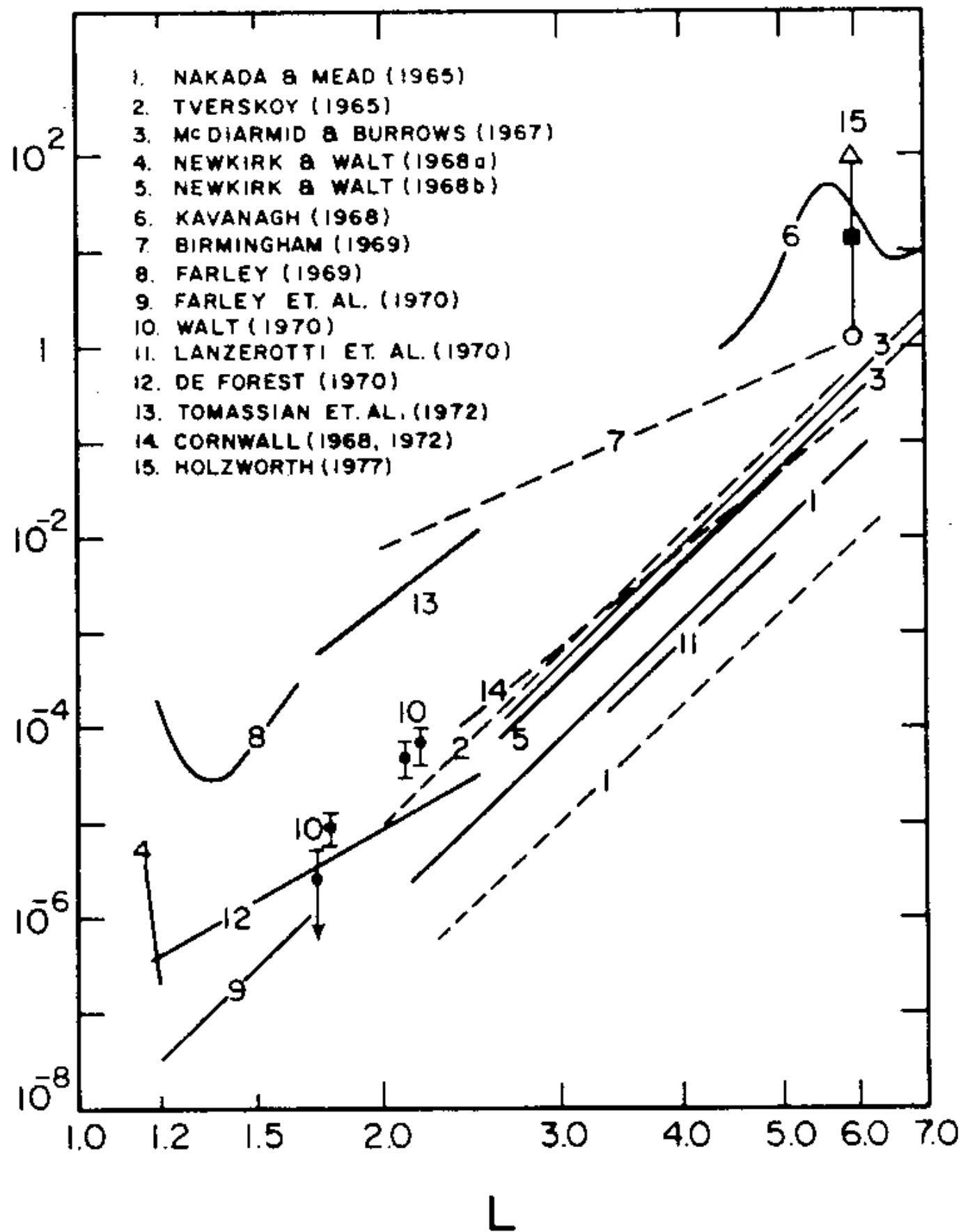
Table 1. Values of coefficients for different pairs of first and second adiabatic invariants.

μ	coeff.	K					
		0.10	0.15	0.20	0.25	0.30	0.50
10.0	b_1	7.28	7.17	7.10	7.50	7.36	6.39
	b_2	4.58	4.63	4.48	4.08	4.16	3.96
	b_3	1.18	1.18	1.20	1.33	1.36	1.52
15.0	b_1	7.30	7.11	7.83	8.05	7.60	6.46
	b_2	4.62	4.57	3.71	3.39	3.54	2.98
	b_3	1.28	1.29	1.42	1.53	1.54	1.72
20.0	b_1	8.26	8.53	8.39	8.66	7.91	6.25
	b_2	3.81	3.18	3.00	2.57	2.64	2.22
	b_3	1.51	1.63	1.66	1.87	1.78	1.93
25.0	b_1	8.17	9.22	8.65	8.47	7.80	6.28
	b_2	3.51	2.20	2.38	2.28	2.17	1.41
	b_3	1.56	1.91	1.90	1.96	1.97	2.24
30.0	b_1	9.11	8.84	8.06	7.40	7.77	4.50
	b_2	2.55	2.18	2.36	2.63	1.68	1.78
	b_3	1.85	1.94	1.89	1.87	2.18	1.60
35.0	b_1	8.66	8.17	5.80	5.55	6.74	3.88
	b_2	2.53	2.34	3.31	3.26	2.02	1.73
	b_3	1.84	1.89	1.21	1.40	2.04	1.87
40.0	b_1	8.22	5.83	5.00	2.77	5.13	3.13
	b_2	2.52	3.29	3.54	4.29	2.56	1.65
	b_3	1.83	1.07	1.15	0.62	1.60	1.96
45.0	b_1	5.97	5.01	3.08	1.43	3.82	2.23
	b_2	3.41	3.55	4.11	4.61	2.72	1.75
	b_3	1.01	0.97	0.59	0.28	1.03	1.85
50.0	b_1	5.78	3.33	-1.82	0.14	2.58	0.45
	b_2	3.38	4.10	5.77	4.97	3.01	2.28
	b_3	1.12	0.49	-1.11	-0.05	0.66	1.06

Table 2. Values of n for different pairs of first and second adiabatic invariants.

		K					
		0.10	0.15	0.20	0.25	0.30	0.50
μ	10.0	-5.0	-5.0	-5.0	-3.5	-4.0	-6.5
	15.0	-5.0	-4.0	-3.5	-2.5	-3.0	-5.0
	20.0	-3.5	-2.5	-2.5	-1.0	-2.0	-4.5
	25.0	-3.0	-1.0	-1.0	-1.0	-1.0	-7.0
	30.0	-1.0	-1.0	-0.5	-1.0	-0.5	1.0
	35.0	-1.0	-0.5	-1.0	-1.0	0.0	0.5
	40.0	-1.0	-1.0	-1.0	-1.5	-0.5	1.0
	45.0	-1.0	-1.0	-1.5	-2.0	0.0	0.5
	50.0	-1.0	-1.5	-2.0	-2.0	-0.5	0.5

$$D = \langle (\Delta L)^2 \rangle / 2 (\text{Day}^{-1})$$



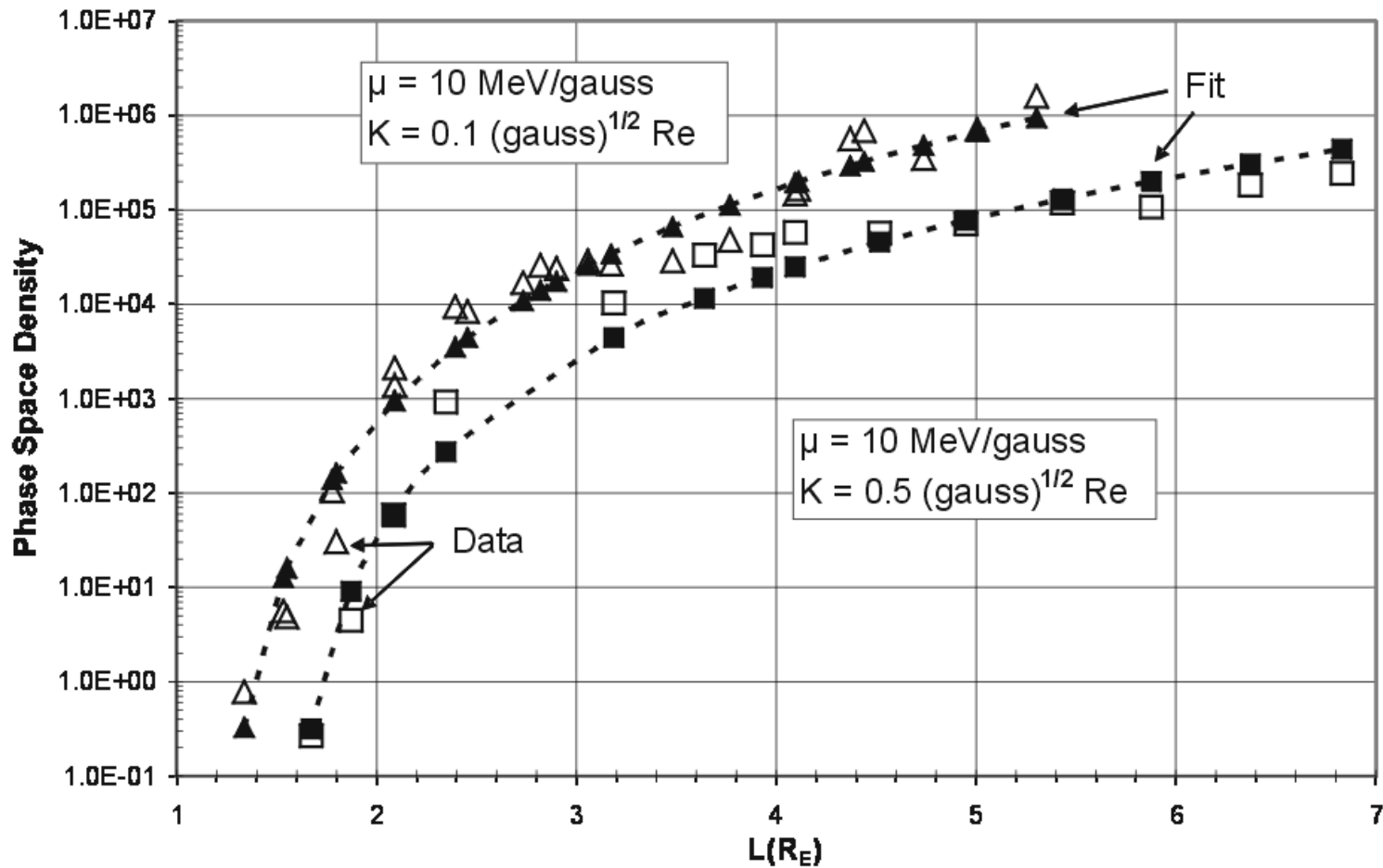


Figure 2

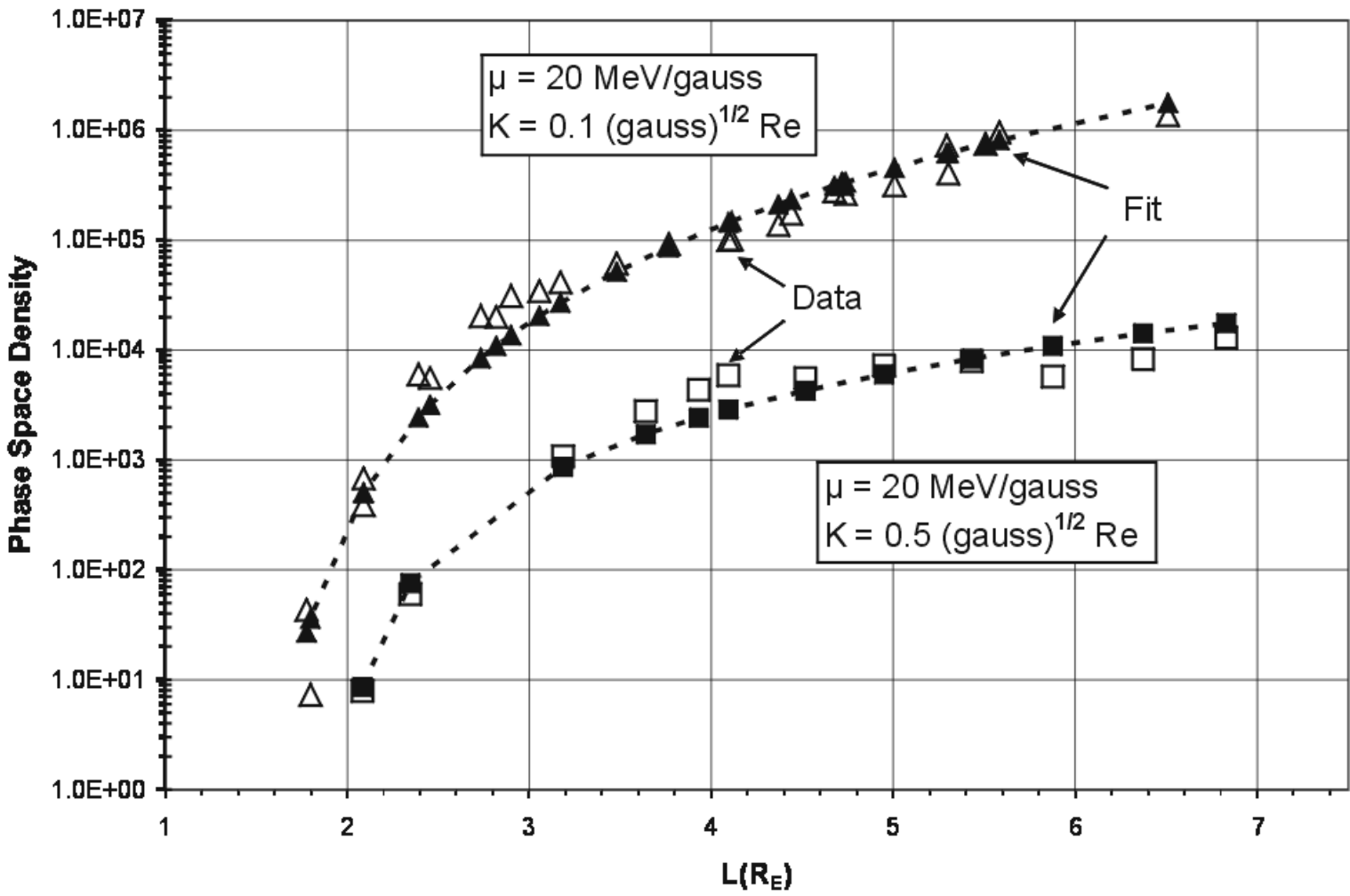


Figure 3

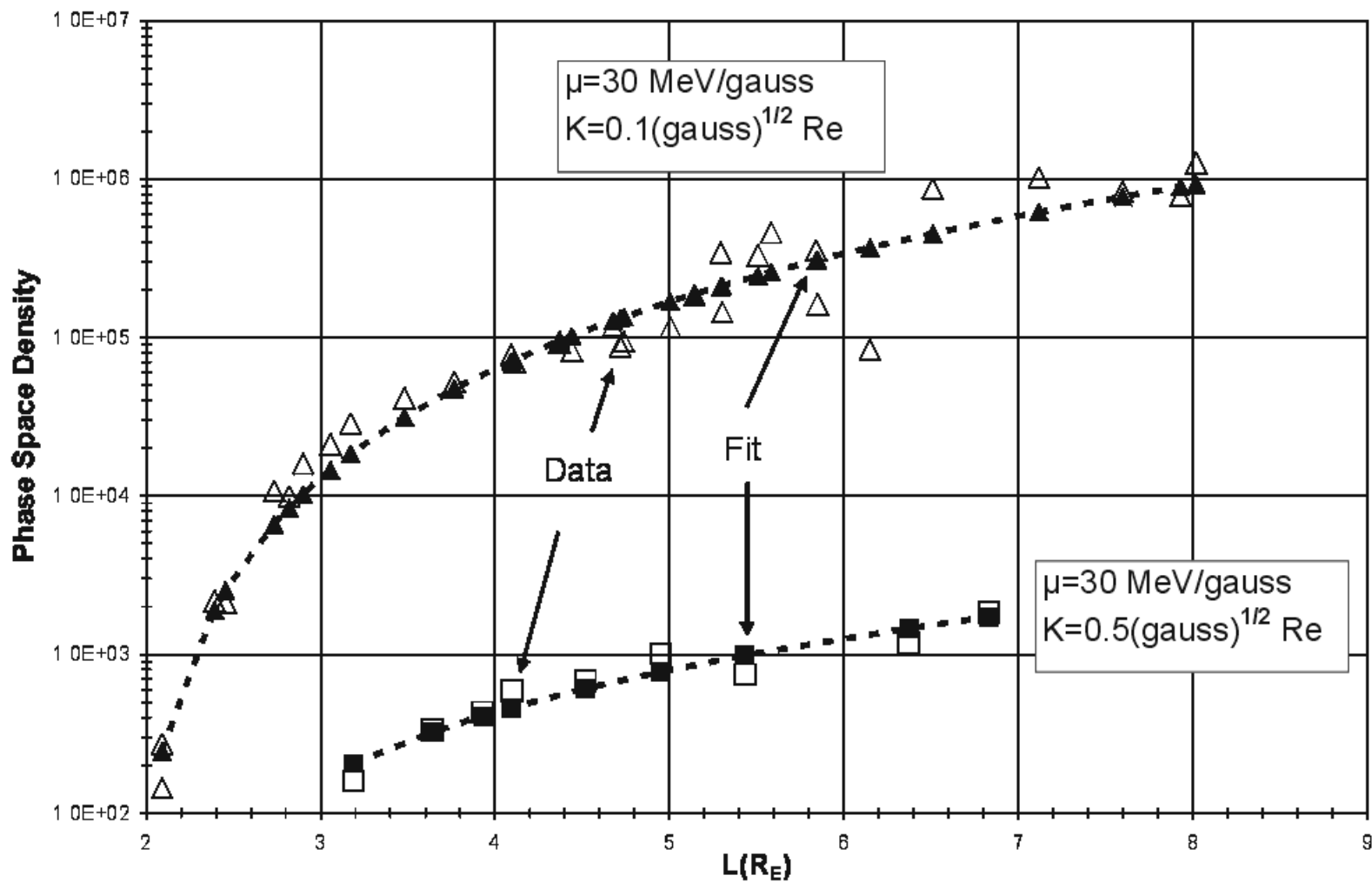


Figure 4

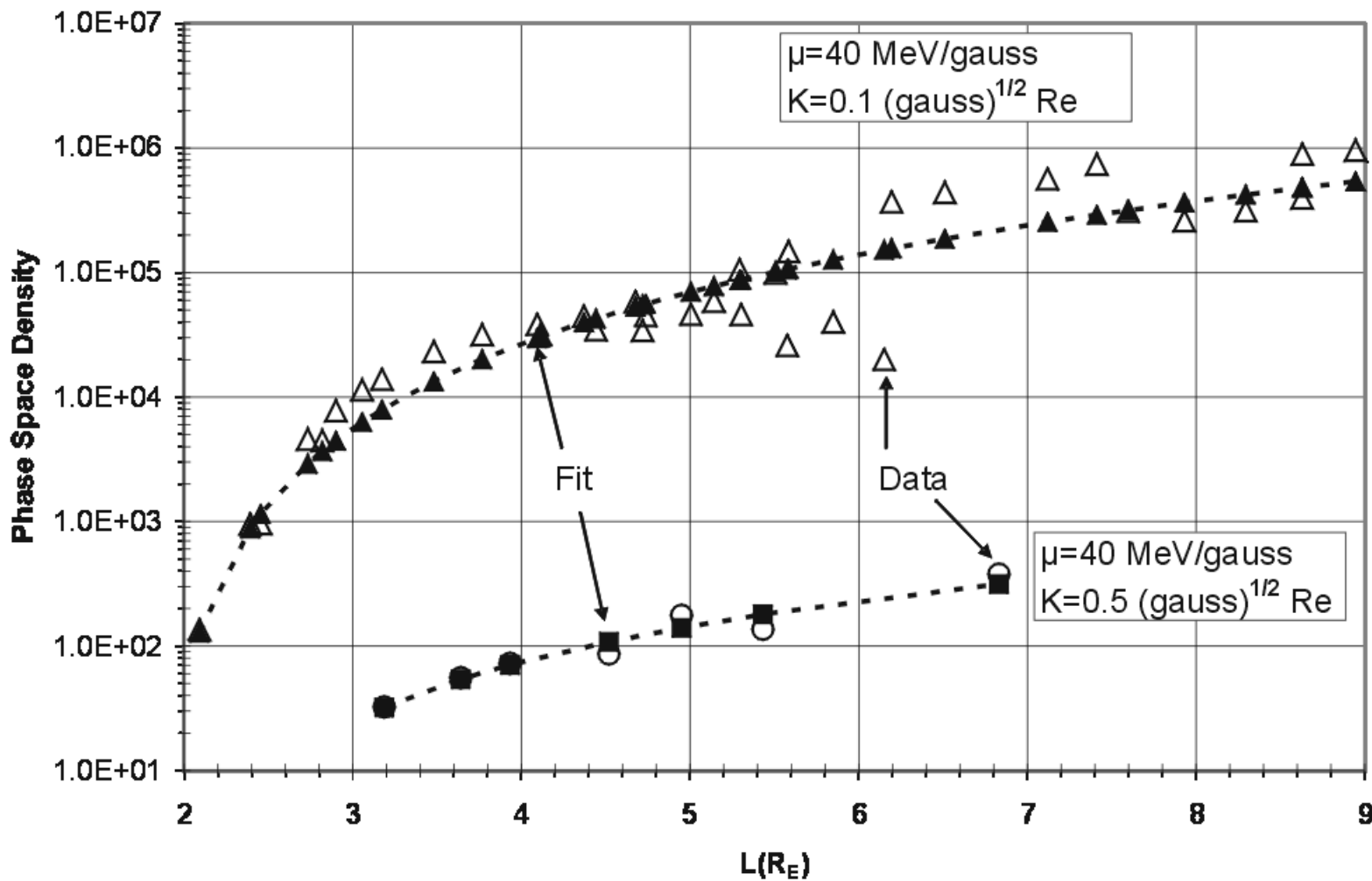


Figure 5

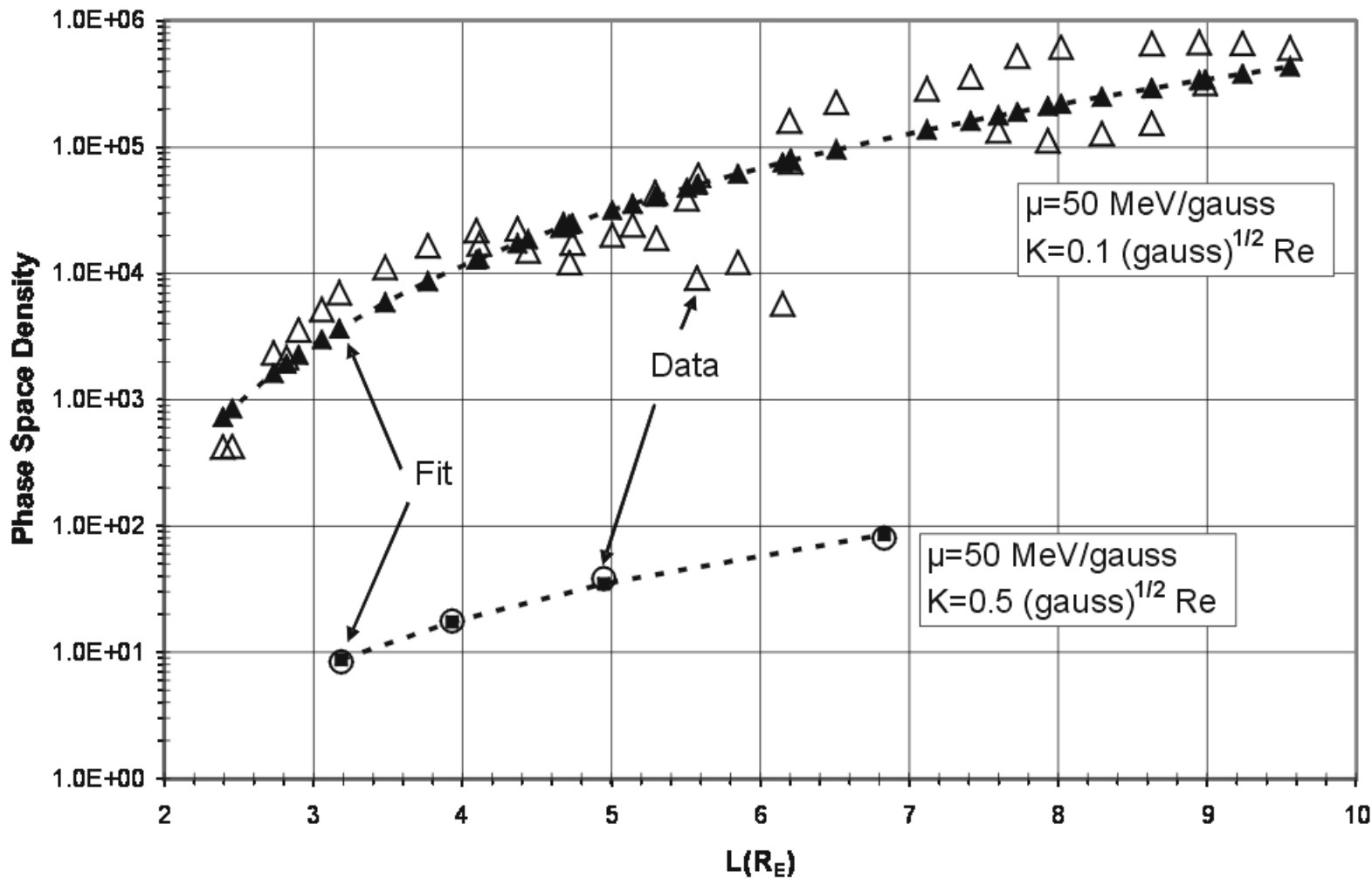


Figure 6

PSD level

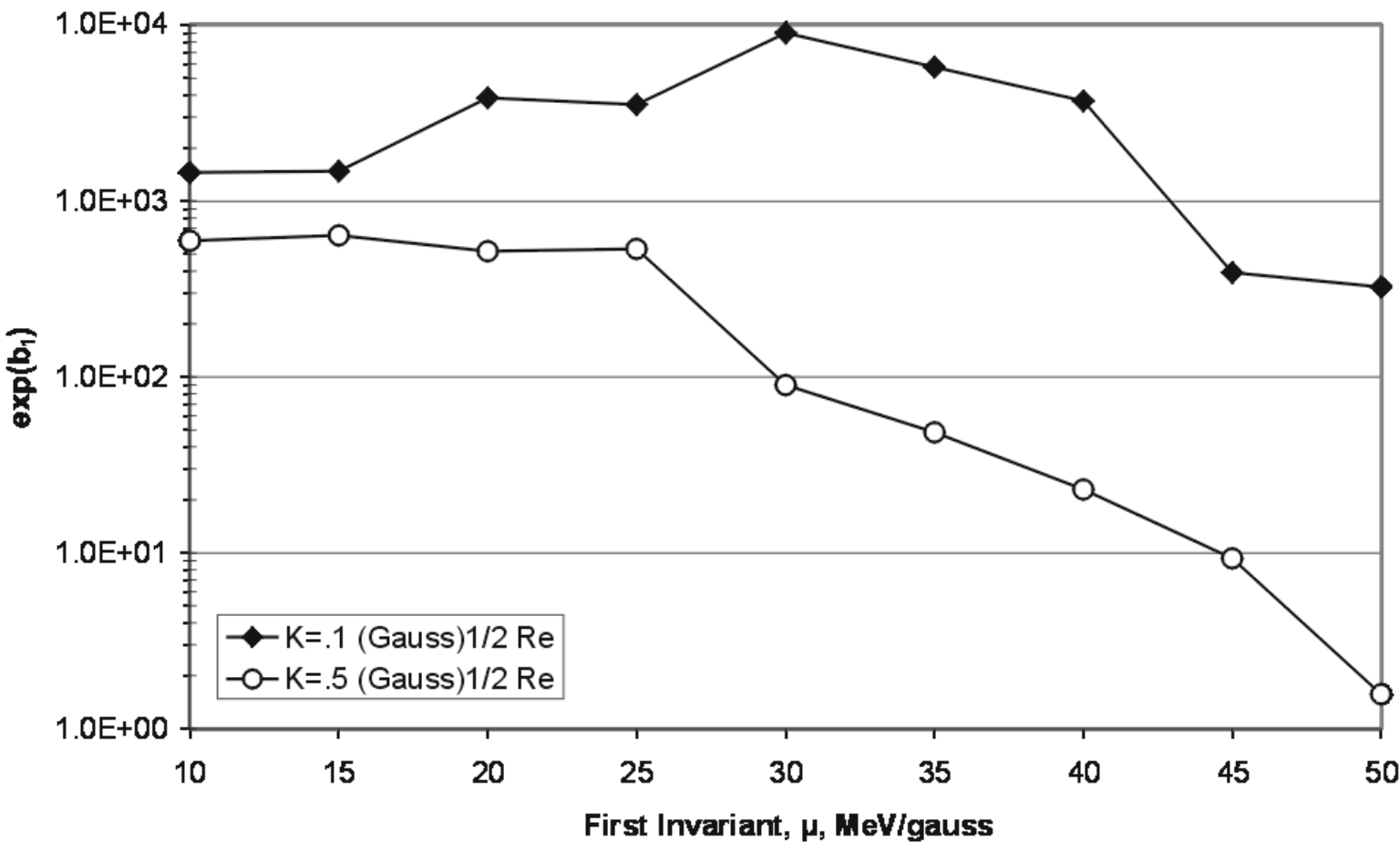


Figure 7

Exponent of PSD L-dependence

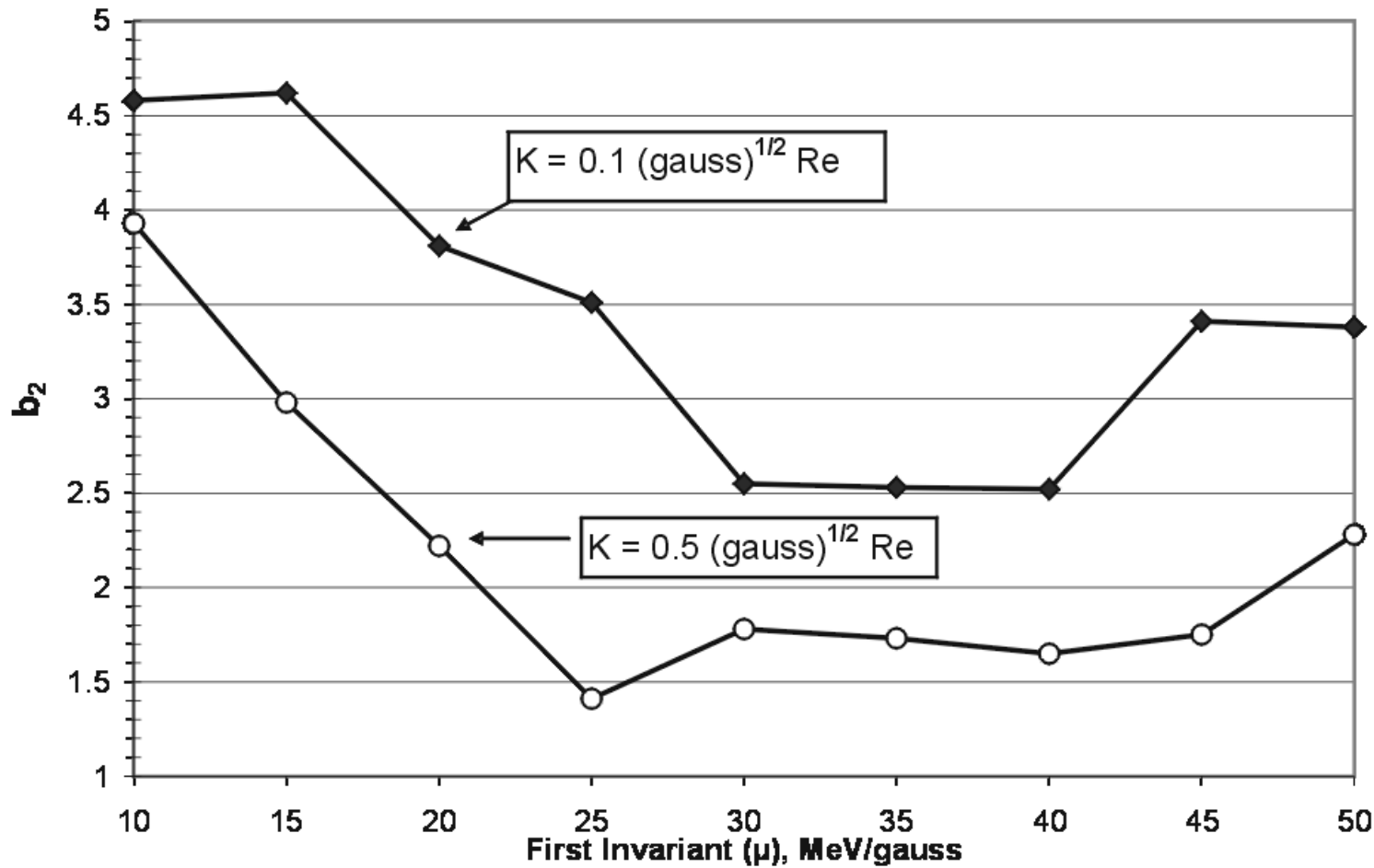


Figure 8

L offset

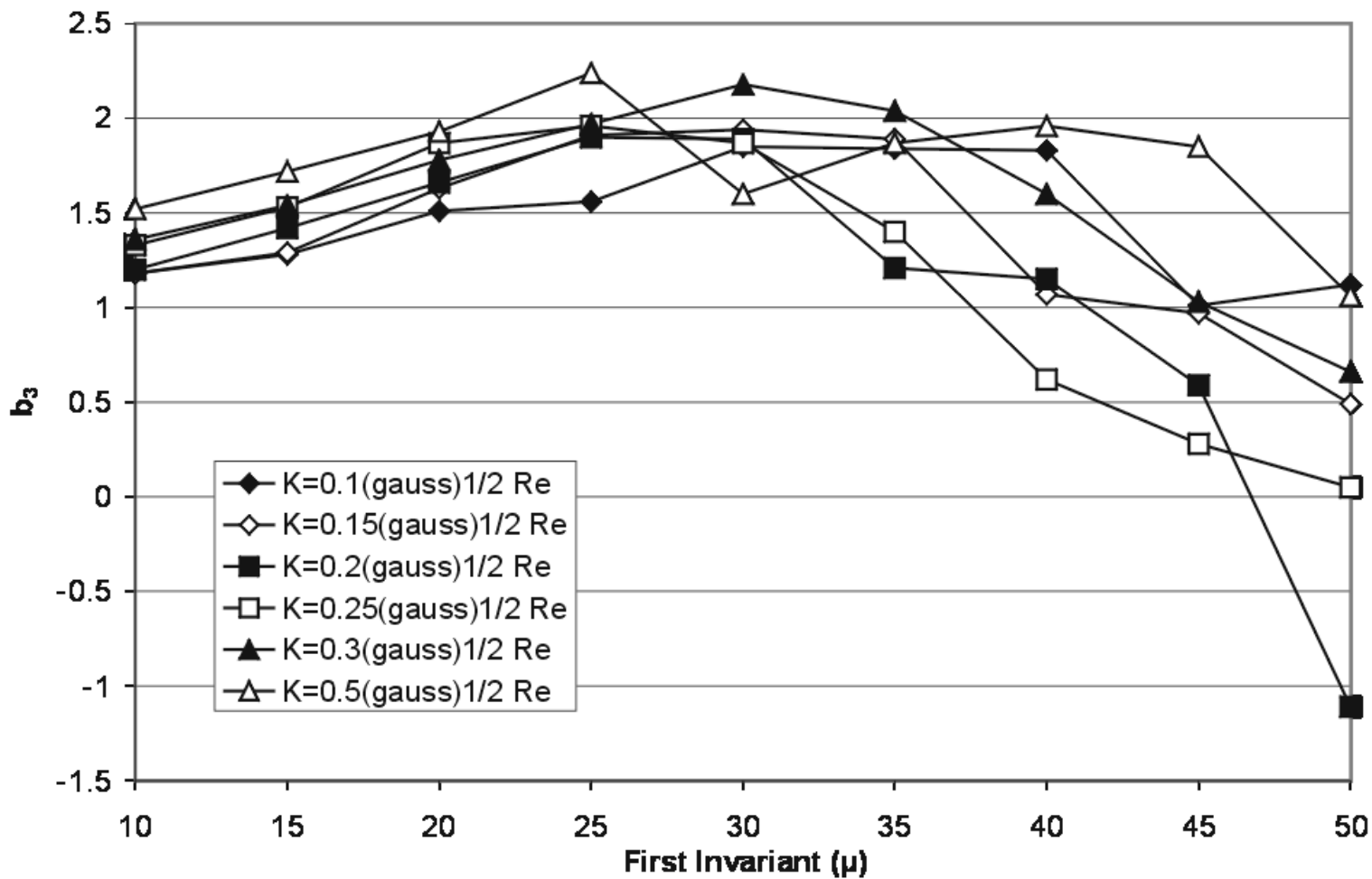
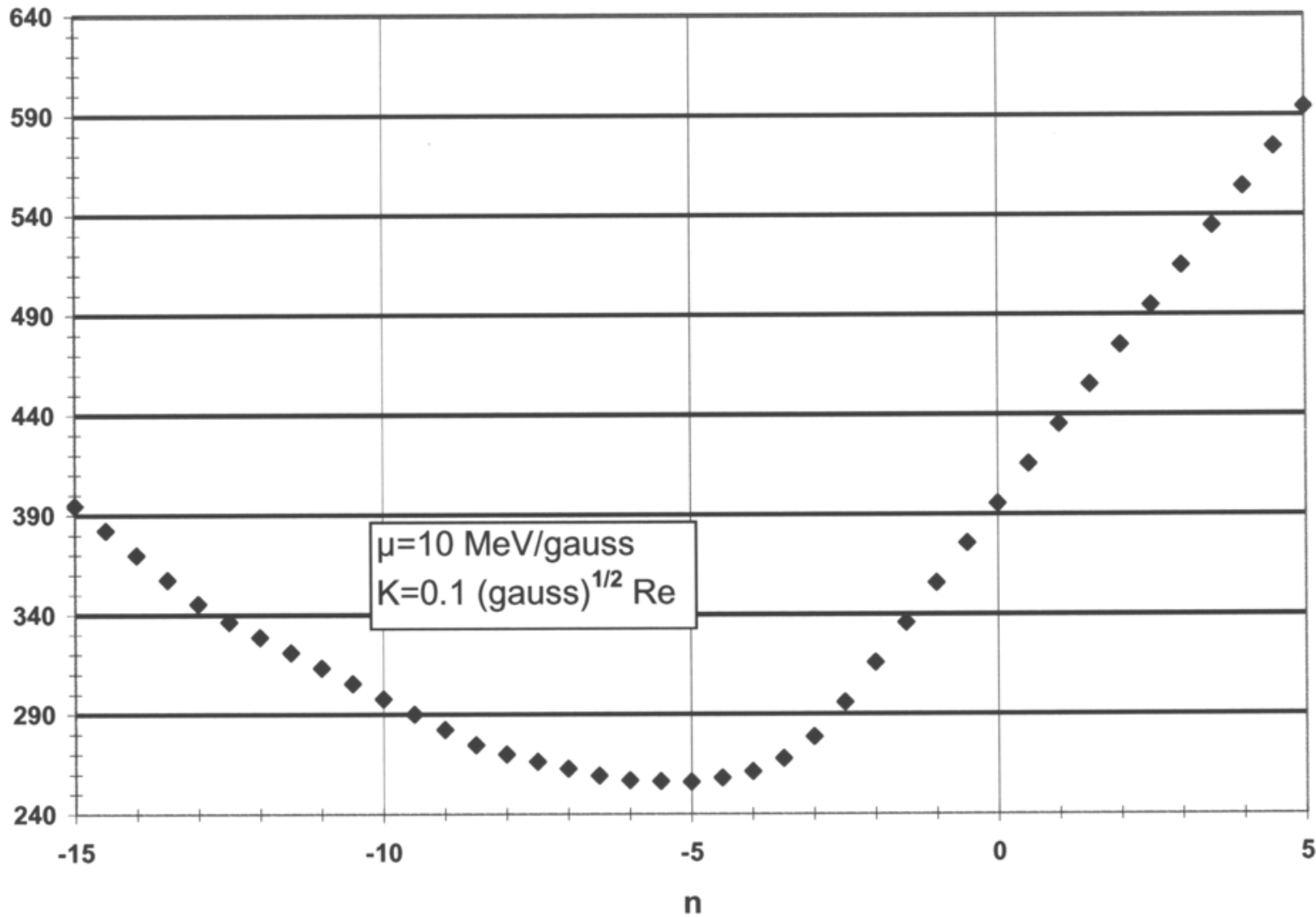


Figure 9

$\Sigma(|b+\ell|)*L^2*\Delta L$ 

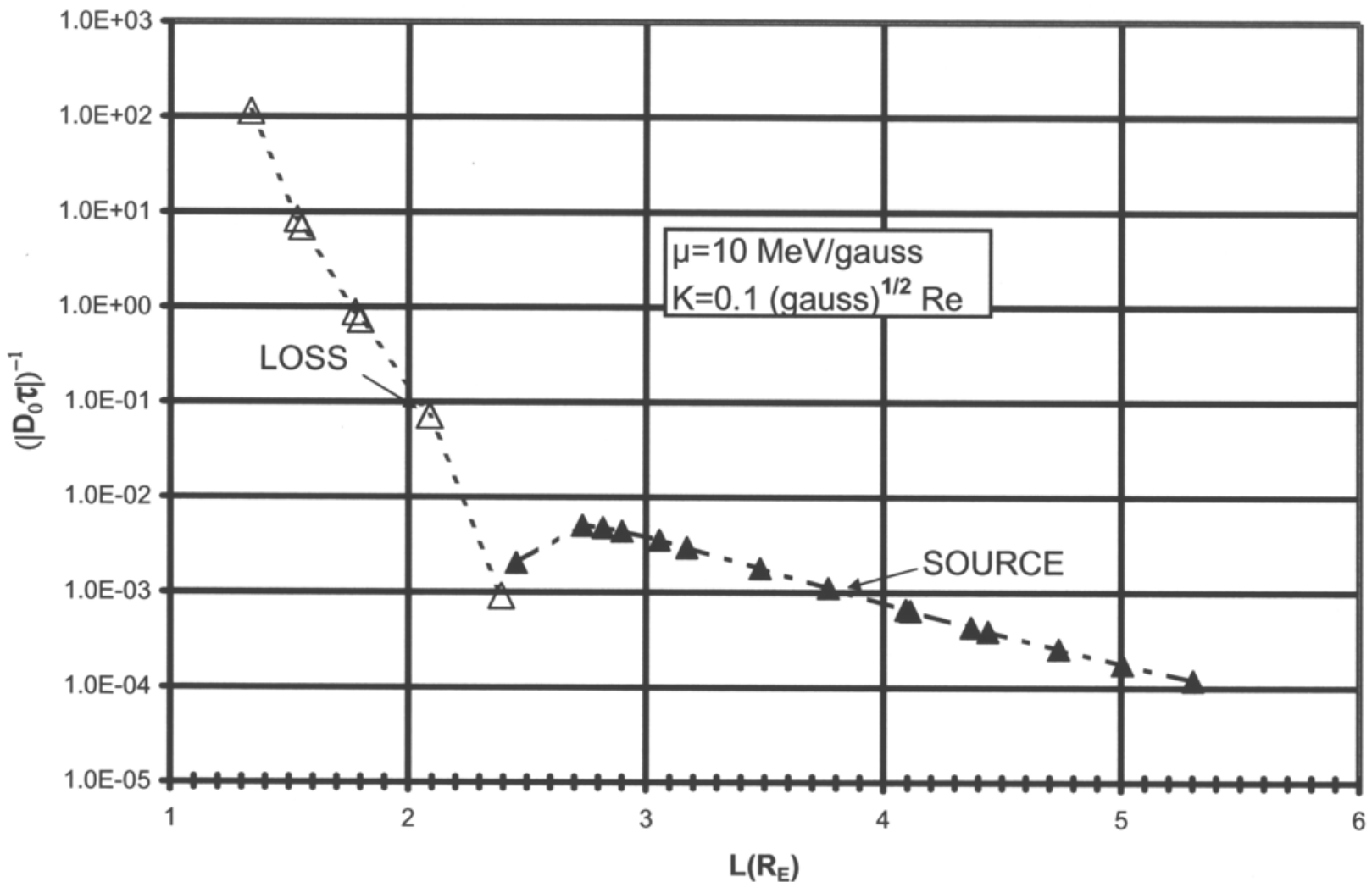


Figure 11

Exponent of D_{LL} Dependence on L

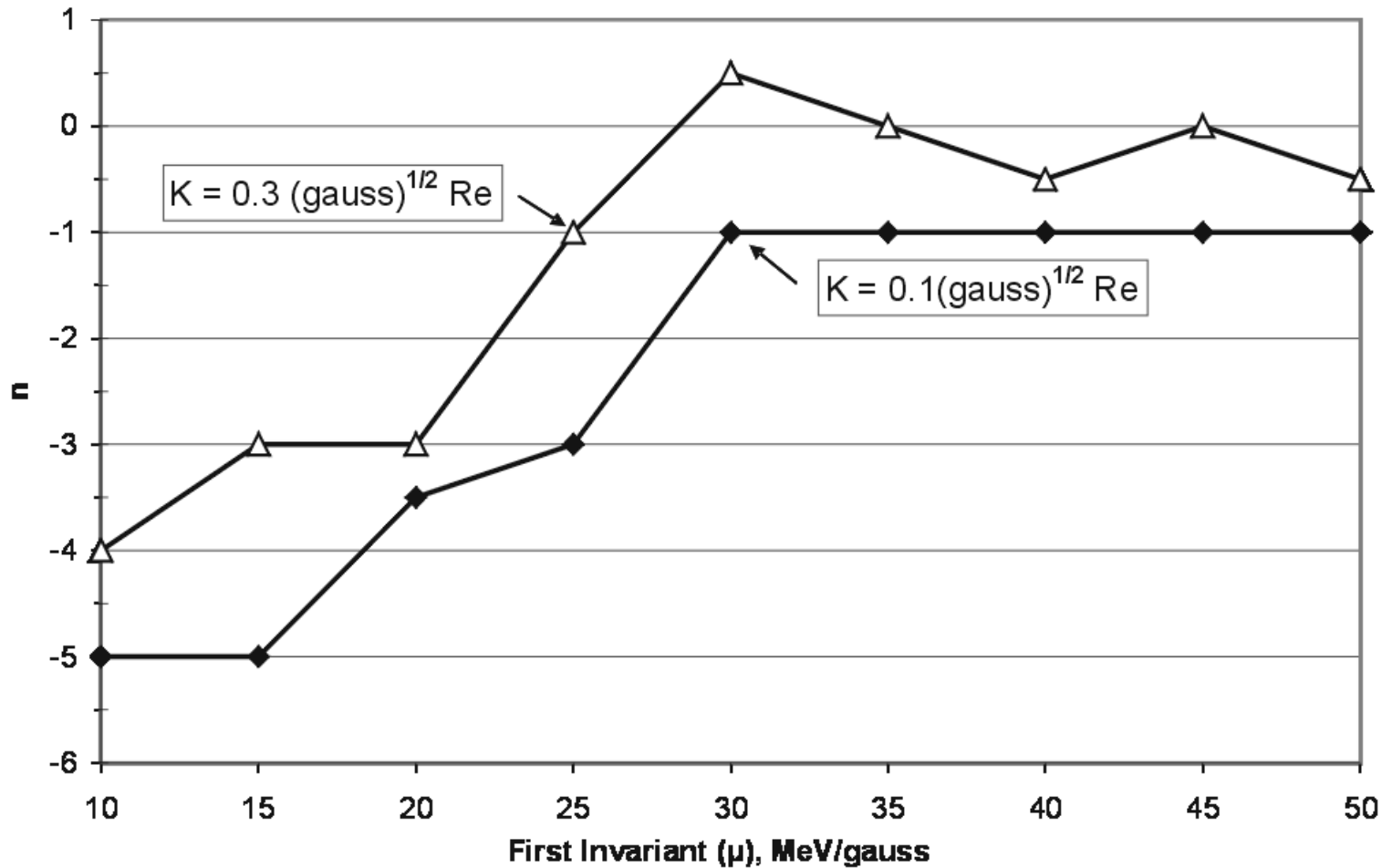


Figure 12

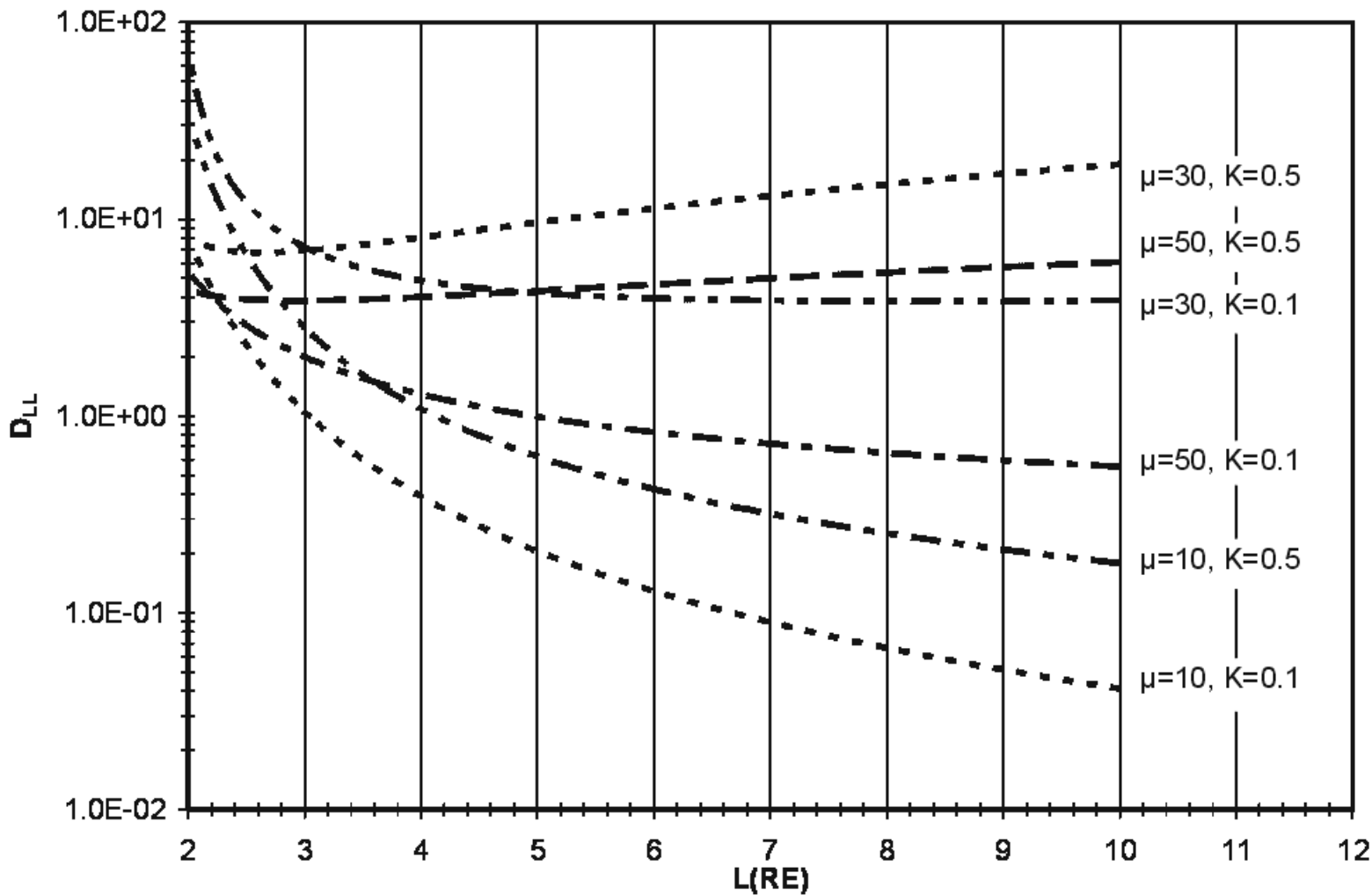


Figure 13